Plasma Chemistry and Plasma Processing (2020) 40:1145–1162
https://doi.org/10.1007/s11090-020-10096-w

ORIGINAL PAPER

Laser Induced Dielectric Breakdown for Chemical Vapor Deposition by Hydrogen Reduction of Volatile Boron Halides BCl_3 and BF_3

I. B. Gornushkin[1] · P. G. Sennikov[2] · R. A. Kornev[2] · A. A. Ermakov[2] · V. E. Shkrunin[2]

Received: 20 April 2020 / Accepted: 4 June 2020 / Published online: 9 June 2020

Abstract
A possibility of deposition from laser-induced plasma is investigated in search for an economic and simple method for obtaining isotopic compounds from enriched gaseous precursors although no isotopic compounds are used in this the proof-of-principle work. A breakdown in mixtures of BCl_3 and BCl_3 with hydrogen, argon, and methane are studied both theoretically and experimentally. Equilibrium chemistry calculations show the deposition of boron, boron carbide, and carbon is thermodynamically favorable in BCl_3 systems and only carbon in BF_3 systems. Dynamic calculation of expanding plasma is performed using fluid dynamics coupled with equilibrium chemistry. Condensed phases of boron, boron carbide, and graphite are predicted with maximum concentrations in peripheral zones of the plasma. In experiment, plasma is induced in mixtures BCl_3, H_2+BCl_3, $H_2+Ar+BCl_3$, $H_2+BCl_3+CH_4$, BF_3, H_2+BF_3, $H_2+Ar+BF_3$, and $H_2+Ar+BF_3$. The gases are analyzed before, during, and after laser irradiation by optical and mass spectrometry methods. The results show the composition of reaction products close to that predicted theoretically. The conversion of precursor gases BCl_3 and BF_3 into gaseous and condensed products is 100% for BCl_3 and 80% for BF_3. Solid deposits of up to 30 mg are obtained from all reaction mixtures. Due to technical reasons only FTIR characterization of the $BCl_3+H_2+CH_4$ deposit is done. It points to presence of condensed boron and boron carbide predicted by the model. Overall, the calculations and preliminary experimental results imply the chemical vapor deposition with laser induced plasma is promising for conversion of gaseous enriched precursors into elemental isotopes and their isotopic compounds.

Keywords Chemical vapor deposition · Laser induced dielectric breakdown · Hydrogen reduction · Boron halides

✉ I. B. Gornushkin
igor.gornushkin@bam.de

[1] BAM Federal Institute for Materials Research and Testing, Richard-Willstätter-Strasse 11, 12489 Berlin, Germany

[2] G.G. Devyatykh Institute of Chemistry of High-Purity Substances of RAS, 49 Tropinin Str., Nizhny Novgorod, Russia 603951

Introduction

Plasma enhanced chemical vapor deposition (PECVD) is a well-established technique for production of thin films [1], protective coatings [2], carbon-based nanostructures [3], high purity isotopic materials [4], biomaterials [5], and many other products [6]. The method is based on using plasma to create unstable bonding states in a precursor gas and activate chemical reactions. In comparison with the traditional chemical vapor deposition (CVD), PECVD exhibits significantly higher deposition rate and ability of working under both low and high pressure conditions. Ways of production of plasma may vary widely depending on an application. Plasmas created in various discharges like DC and AC glow discharges or discharges operated at audio (10–20 kHz), radio (13.56 MHz), and microwave (2.45 GHz) frequencies are typically used. It can also be a laser induced dielectric breakdown (LIDB) plasma created on a suitable substrate or in a precursor gas. Namely this type of plasma for CVD is the subject of this paper.

There are several laser-assisted CVD techniques that do not exploit laser breakdown. The method of laser-induced CVD, LCVD (commonly referred to as direct laser writing [7]), uses lasers to decompose the reactant gas by either thermal effects (pyrolytic LCVD) or resonance absorption of laser light (photolytic LCVD) [8]. In contrast to LIDB CVD, LCVD is a well-developed technique. For example, pyrolytic LCVD was used to produce polycrystalline Si by thermal decomposition of $SiCl_4$ [9] and SiH_4 [10] by heating the substrates by either CO_2 or Ar^+ lasers. Photolytic LCVD was employed to obtain silicon [11] and germanium [12] films by photodecomposition of precursor gases by CO_2 lasers.

The method of LIDB CVD is simple instrumentally and able to provide higher deposition rates than PECVD and LCVD methods. The radiation from a pulsed laser is focused above a cold substrate surface to create dielectric breakdown in the precursor gas. The localized reaction zone with high temperature is formed above the low-temperature substrate surface providing the high quench rate favorable for deposition. Jervis [13] has efficiently produced nickel films on glass substrate by focusing a pulsed CO_2 laser into the laminar flow of nickel tetracarbonyl, $Ni(CO)_4$, mixed with argon. Deposition occurred very rapidly at a rate of 5–10 Å per pulse so that a visible film of Ni formed in just a few minutes at the laser repetition rate of 0.5 Hz. The compositional analysis revealed incorporation of about 10% carbon in the film. Similarly, the films of Mo and W from the $Mo(CO)_6$/Ar and WF_6/H_2/Ar precursor gases were obtained using LBCVD [14]. The films were not the same pure as Ni films and contained 30% C and 30% O for Mo and 41% O and 6% N for W. The formation of ultrafine particles via LIDB CVD with the CO_2 laser has been reported by Ronn and colleagues [15, 16]. The iron particles were produced from ferrocene $Fe(C_5H_5)_2$, molybdenum from carbonyl $Mo(CO)_6$, and sulfur from OCS and SF_6/H_2. Draper [17] has produced ultrafine (< 100 Å) elemental metal powders from Fe, Cr, Mo, and W carbonyl vapors by LIDB CVD with the CO_2 laser. The result also suggested the possibility of production of alloyed powders by mixing carbonyl vapors. This idea was later realized by Shin et al. [18] who obtained very fine (< 100 Å) Cr–Mo–W alloy powder particles by CO_2 laser breakdown in a mixture of the corresponding metal carbonyl vapors. Draper [19] has also reported the formation of "cobwebs" of molybdenum metal by the CO_2 laser LIDB in the mixture of molybdenum hexacarbonyl and the long straight-chained hydrocarbons.

Since the 1980th the method of LIDB CVD has been abandoned and publications on this subject disappeared from literature. We cannot give a reason for that and our intention is to revive interest to LIDB CVD. Our main goal is to test this technology for production

of isotopically pure boron, silicon, and germanium and their isotopic compounds from isotopically enriched gaseous precursors, e.g. chlorides and fluorides. These materials are in high demand in numerous fields. For example, boron ^{10}B, ^{11}B, and $^{10}B_4C$ are widely used in nuclear technologies [20, 21] because ^{10}B and $^{10}B_4C$ are the excellent absorbers and ^{11}B is the reflector and decelerator of neutrons. Boron isotopes are demanded in biology [22] and medicine, e.g. in boron neutron capture therapy (BNCT) [23]. Isotopes ^{28}Si and $^{28}Si^{12}C$ are promising as qubits in quantum computers [24–26]; ^{29}Si is an active agent in magnetic resonance tomography (MRT) [27]. Isotopic carbide $^{28}Si^{12}C$ is used for coating nuclear reactor walls. Enriched to 88%, ^{76}Ge is used as a detector in double neutrinoless beta decay experiments [28]. Germanium carbides $Ge_xC_{(1-x)}$ can be used as refractory coatings [29] and wide-bandgap semiconductors [30].

In this paper, we theoretically analyze the possibility of production of boron and its compounds in the condensed phase by LIDB CVD from two precursor gases. The gases are boron halides (chloride and fluoride) mixed with hydrogen, argon, or methane that is typical for PECVD. First, we perform *static* equilibrium chemistry calculations that are valid for both PECVD and LIDB CVD as first approximation. A goal is to see if the condensed phase of boron is thermodynamically favorable. Second, we perform *dynamic* calculations of the expanding laser induced plasma plume using the fluid-dynamics-equilibrium-chemistry code to see in which plasma zones the condensed phase is formed; this may alleviate a construction of LIDB chemical reactor. And third, we carry out the first pilot LIDB CVD experiment with precursor gases BCl_3 and BF_3 mixed with hydrogen, argon, and methane to evaluate the feasibility of this process. The gases and one solid deposit are analyzed by a variety of spectroscopic techniques and the results of experiment are compared to calculations.

Calculation of Chemical Equilibrium

The calculations are performed using open source software [31]. The software implies local thermodynamic equilibrium (LTE) and is based on the Gibbs free energy minimization algorithm

$$\min G(\boldsymbol{n}) = \sum_{j=1}^{N} \mu_j n_j$$

where μ_j and n_j are the chemical potential and number of gram-moles of species j per gram of mixture and N is the number of molecular species. The minimization is subject to the mass balance and non-negative concentration constraints; the minimization is performed by the Lagrangian multipliers method. Abundant literature exists on the topic [32]. We have also recently developed an algorithm based on the mass action, charge and mass conservation lows [33–35]; however, this model does not include the phase transformation processes that are of primary interest in plasma deposition methods.

The model [31] assumes the equation of state for an ideal gas even when small amount of the condensed phase is present. This assumption is acceptable because of the negligible volume of the condensed phase relative to the gaseous species [31]. Another simplification is the purity of the condensed phase; the phase transitions are allowed between liquid and gas, solid and gas, solid and liquid, and between stable solid phases.

First, the plasma composition as a function of temperature is calculated for the *steady* state plasma at fixed pressure of 1 atmosphere, a so-called t-p option in [31]. The plasma is

assumed to be in LTE that is admissible for atmospheric RF arc and ICP [36] plasmas and for laser induced plasma in its late stage. Laser induced plasmas do not always remain at LTE, especially in the first 100 ns after breakdown [37]. In later times, however, after the shocks traveled away, the plume expansion slows down and the characteristic times of the hydrodynamic flow $\tau_\rho = \rho/D_t\rho$ and $\tau_T = T/D_tT$, where D_t is the material time derivative, ρ is the plasma density, and T is the temperature, become larger than a characteristic time for chemical reactions. If, in addition, the number densities are sufficiently high, then the assumption of LTE is reasonable [38]. There is a more elaborate set of sufficient conditions under which plasma may be viewed as near LTE [39, 40].

Second, the *dynamic* composition of the laser-induced plasma plume expanding in a gas atmosphere is calculated by embedding the chemical code [31] into the hydrodynamic code developed by us earlier [33–35]. LTE is assumed for both plasma chemistry and plasma dynamics. A collisional-dominated model is based on the coupled Navier–Stokes, state, radiative transfer, material transport, and chemical equations. The model incorporates plasma chemistry through the equilibrium approach that relies on the minimization of Gibbs free energy approach. Both 1D (spherical symmetry) and 2D (cylindrical symmetry) calculations are carried out to reveal zones of formation of condensed matter in recombining and chemically-active laser induced plasma.

Experiment

The sketch of the experimental set-up and the photo of the laser induced breakdown in the H_2/BCl_3 gas mixture are given in Fig. 1. A pulse from a Nd:YAG laser at the fundamental wavelength of 1064 nm with a 15 ns duration, 800 mJ pulse energy, and 5 Hz repetition rate was focused inside the enclosure by a 5 cm focal length lens. A fluence in the focal point was 26 J cm^{-3}.The enclosure, a fixed volume chemical reactor, was a sealed quartz cylinder of length 17 cm and diameter 3.5 cm. Inside the cylinder, another cylinder was placed of diameter 1.8 cm that served as a substrate for reaction products with a deposition area of 8 cm^2. The reactor was loaded with gases shown in Table 1.

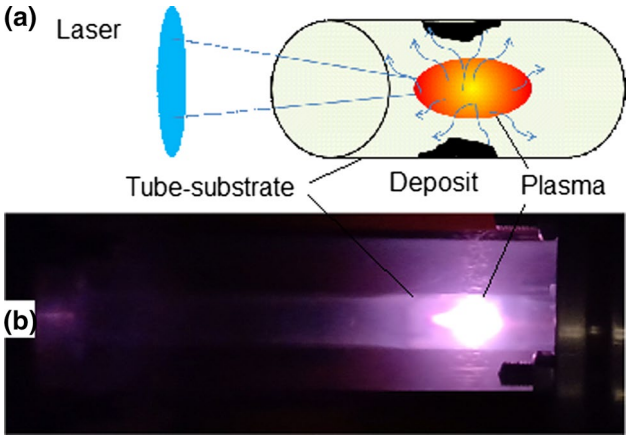

Fig. 1 **a** schematic of chemical reactor based on laser induced plasma; **b** photo of laser induced plasma in H_2:BCl_3 mixture

Table 1 Gases used in experiment

№	Gas	Stoichiometry
1	BCl_3	1
2	H_2:BCl_3	10:1
3	H_2:Ar:BCl_3	10:10:1
4	H_2:BCl_3:CH_4	9:1.5:1
5	BF_3	1
6	H_2:BF_3	3:1
7	H_2:Ar:BF_3	3:4:1
8	H_2:BF_3:CH_4	9:1.5:1

The mixtures were at atmospheric pressure and prepared by volumetric mixing gases via flow regulators PPG-10 and PPG-12 (Eltochpribor). A laser spark had an ellipsoidal shape with longitudinal and transversal dimensions of 1 cm and 0.2 cm, correspondingly. A deposit was either thin film or powder. A mass of the deposit was between 0.003 g and 0.06 g. Deposits were obtained by running the laser up to 50 min thus delivering up to 15,000 laser shots into the reactor volume.

The composition of a plasma and efficiency of conversion of boron halides into gaseous and condensed products were investigated by optical emission spectrometry (OES), infrared (IR) spectrometry, and mass spectrometry (MS). In OES, light from the plasma was collected through the reactor wall by a lens, focused to a fiber, and delivered to a dispersion spectrometer (AvaSpec-ULS3648-USB2-UA-25c). A spectral range was 200–900 nm with resolution 1 nm.

IR spectra of gaseous components before and after irradiation were recorded in range 450–7000 cm^{-1} by an IR spectrometer (BrukerVertex 80v) and detector DTGS. Entrance aperture of the spectrometer was 0.5 cm and resolution 1 cm^{-1}. For analysis, gas from the reactor was taken to a cell of optical path 10 cm. Pressure in the cell was between 20 and 200 torr. The conversion grade was calculated from intensity ratios of vibration bands of various molecules.

MS spectra of gaseous components before and after irradiation were measured by a quadrupole mass-spectrometer (ExtorrXT300(M) SeriesRGA) of resolution 1 amu. Working pressure of an analyte gas was between 10^{-6} and 10^{-5} torr and residual pressure inside the spectrometer was 5×10^{-8} torr. Conversion efficiency was calculated from ratios of most intense lines in a mass spectrum.

The IR spectrum of one of the solid deposits was measured by a FTIR spectrometer (Tensor-27, Bruker) with a cooled DTGS detector. The spectrometer was coupled to a IR microscope (HYPERION 2000) of magnification 15× and numerical aperture NA = 0.4; spectral resolution was 4 cm^{-1}.

Results and Discussion

Static Simulations at LTE

Static equilibrium chemistry calculations are performed for samples № 3, 4 and 7, 8 in Table 1 but for slightly different stoichiometry of components (see figure's caption).

These calculations are in first approximation valid for both PECVD and LIDB CVD and their goal is to verify that condensed phases of boron and other components are thermodynamically favorable with different chemical systems at various temperatures and atmospheric pressure.

Figure 2 shows the equilibrium distribution of plasma species as a function of temperature for the mole ratios BX_3:H_2:Ar = 1:19:45, X = Cl, F recommended in [41] for PECVD. For system BCl_3:H_2:Ar (Fig. 2, a, the condensed boron (both solid and liquid) with the molar concentration of up to 3% is created within temperature range 800–3000 K Also, significant amount of gaseous boron, up to 1%, is produced at temperatures > 3000 K. Note, at temperatures between 2500 K and 3000 K liquid and gaseous boron coexist and the fraction of gaseous boron increases with increasing the temperature. This is due to the increase in density of saturated vapor of boron and production of additional gaseous boron as a result of decomposition of radicals BH_2Cl, $BHCl_2$, and BCl_2. The similar yield of the condensed and gaseous boron in the same reaction mixture was predicted with the hybrid model in [41] that included gas equilibrium chemistry and solid diffusion transport. The concentrations of species at high temperatures > 3000 K predicted by the present model and model [41] coincide with that of the model [42, 43], which are based on solely the *gas* reaction chemistry. For system BCl_3:H_2:CH_4 (Fig. 2b), efficient conversion of BCl_3 into condensed B_4C is accompanied

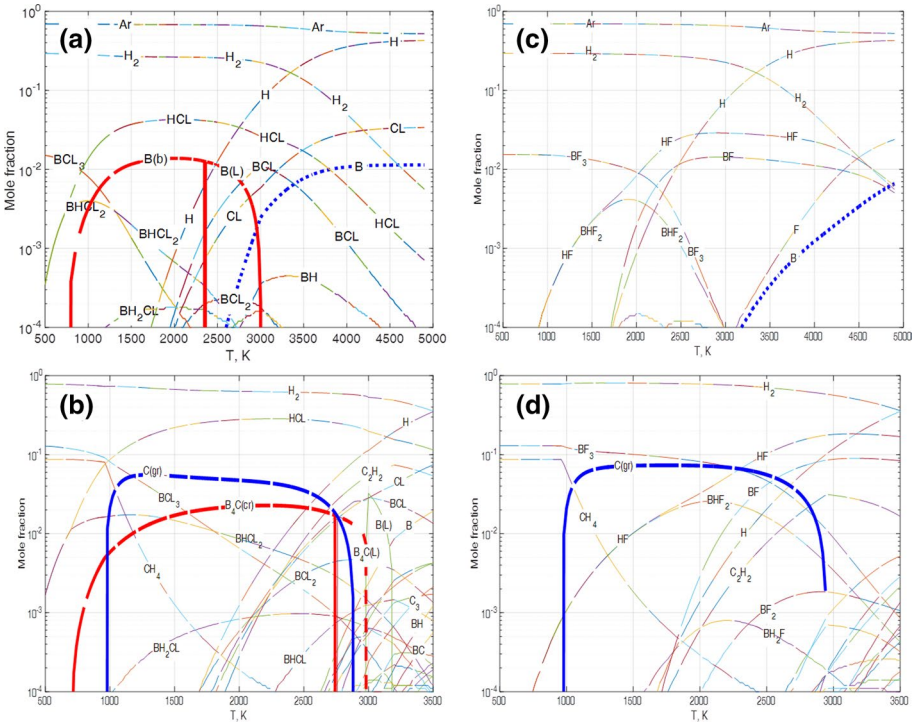

Fig. 2 Comparative calculations of molar fractions as a function of temperature at equilibrium for **a** $BCl_3 : H_2 : Ar = 1 : 19 : 45$ as in [41]; **b** $BCl_3 : H_2 : CH_4 = 1.5 : 9 : 1$ as in [45]; **c** $BF_3 : H_2 : Ar = 1 : 19 : 45$; and **d** $BF_3 : H_2 : CH_4 = 1.5 : 9 : 1$ at atmospheric pressure

by formation of solid graphite. For comparison, formation of B_4C from BCl_3 at low pressure was also predicted in [44] using the chemical kinetic approach.

For mixture BF_3:H_2:Ar (Fig. 2c), the equilibrium model does *not* predict the condensed phase of boron; only gaseous boron appears at temperatures > 3500 K at amounts ~ 0.1%. This result also coincides with that of [41]. For system BF_3 : H_2 : CH_4 (Fig. 2d), only condensed phase of graphite forms, no other boron-containing solid components are observed. A comparison of the equilibrium calculations with kinetic calculations in [44] and experiment [45] implies that the formation of boron carbide at high (> 1000 K) temperatures is a complex process that cannot be fully described by equilibrium chemistry. The latter only provides a general trend in evolution of chemical systems as pressure, temperature, and stoichiometry of species are varied. There exist other works where boron and boron carbide were obtained from BF_3 and hydrocarbons by PECVD in radio (13.56 MHz) and microwave (2.45 GHz) frequency discharges (e.g. [46]).

Dynamic Simulations of LIDB at LTE

Chemistry in transient reactive plasma like LIDB (laser-induced dielectric breakdown) is modeled by either using a concept of LTE or a collisional-radiative model (CRM) [47, 48] and state-to-state approach [49, 50], both combined with computational fluid dynamic, CFD. In equilibrium models, the plasma is assumed to be an isolated system in which LTE is established between neutral and charged particles and gaseous and condensed phases. A thermodynamic state of such the system is determined by concentrations of chemical elements and state variables.

For solving the multi-reaction equilibrium, hierarchical algorithms are often used [51–53]; their accuracy critically depends on the correct choice of a subset of molecular species from which all other species are formed by chemical reactions. Another way to solve the multi-reaction equilibrium is to minimize Gibbs free energy of a chemical system under the LTE assumption [54]. Owing to its clear physical sense and enormous database of thermodynamic functions available for various compounds, this approach became very popular. A comprehensive review of numerical methods related to chemical reactors can be found in [55, 56].

Using a kinetic model, e.g. the one proposed in [44] for the $BCl_3/CH_4/H_2$ system, is not always possible due to lack of chemical kinetic reaction data. Rates for direct and backward reactions can be obtained by either ab initio calculations or approximation through thermochemical data (entropy, enthalpy, and heat capacity). Ab initio calculations can be time-prohibitive while their accuracy depends on a level of theory; approximations via interpolation or extrapolation of experimental data are also imprecise. A main advantage of kinetic calculations, however, is in its ability of modeling non-equilibrium plasma conditions, an option that is unattainable by the Gibbs energy minimization approach. Nevertheless, the latter remains often the only choice because many rate coefficients are not in the literature or cannot be computed as, e.g., is the case with the $BF_3/CH_4/H_2$ system, which is studied in this work.

Dynamic calculations of the expanding plasma plume are carried out using the fluid dynamic code [33–35] coupled to the equilibrium chemistry code [31]. The goal is to see, when, under what conditions (pressure, temperature), and in which plasma zones the condensed phase (or phases) is formed. The simulations may help to choosing the correct geometry of a LIDB reactor and optimizing experimental conditions.

Preliminary calculations are performed for plasmas in spherical (1D) and cylindrical (2D) symmetries. Figure 3c, d show the results of the 1D calculations for system 50% Ar + 50% (BCl_3:H_2 = 1:10) and e, f for system 50%(CH_4:Ar = 3:1) + 50% (BCl_3:H_2 = 1:9). Proportions of gases were chosen based on PECVD experiments with RF discharges. For both the cases, calculations were started at initial temperature around 5000 K and density equal to the density of the gas in the volume of the initial plasma plume at normal conditions (room temperature and atmospheric pressure). The entries for both the hydrodynamic code and NASA CEA chemical solver [31] were of a u–v type, i.e. the internal energy—gas density type. The initial internal energies were $5 \times 10^4 ergcm^{-3}$ and $2 \times 10^4 ergcm^{-3}$ for 1D and 2D simulations, correspondingly that provided the initial plasma temperature around 5000 K in both cases. Spatial distributions for both density and internal energy were taken uniform over the volume of the plasma plume at zero time. For spherical (1D) expansion, the initial plasma radius was 0.4 mm and for the initial ellipsoidal (2D) plasma, the semi-axes were 0.6 mm and 0.3 mm. A numerical convergence was tested and reached at a time step of 1 ns and a spatial step of 2.5×10^{-4} cm for the 1D plasma (the thickness of spherical layers) and 3.8×10^{-4} cm for the 2D plasma (the thickness of ellipsoidal layers). It is worth noting that the initial plasma temperature did not reflect physical reality. Typically, plasma temperature at the onset of laser breakdown reaches 10's thousands of K and drops to ~ 10,000 K within several hundreds nanoseconds. We chose such the low initial temperature in order to faster reach conditions at which molecules and condensate form and thus save much computational time. At $T \gtrsim 6000$K not much chemistry occurs as only rare

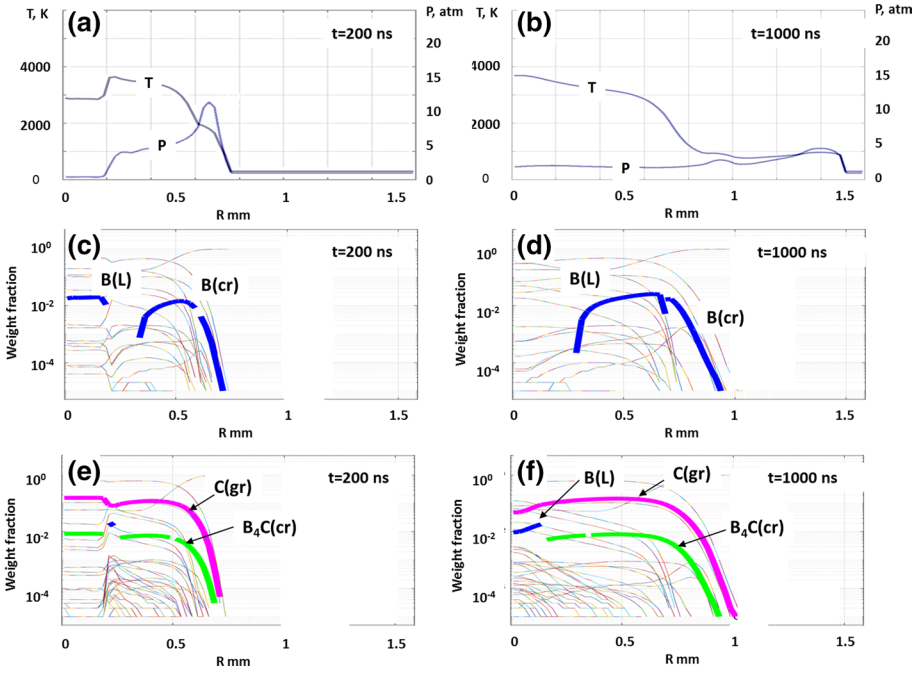

Fig. 3 Dynamic simulations of 1D spherical laser induced plasma; **a** temperature and pressure profiles at 200 ns of simulation time; **b** the same profiles at 1000 ns of simulation time; **c** 50% (Ar) + 50% ($BCl_3 + H_2$): snapshot of concentrations at 200 ns; **d** same system, snapshot at 1000 ns; **e** 50% (CH_4 + Ar) + 50% ($BCl_3 + H_2$): snapshot at 200 ns; **f** same system, snapshot at 1000 ns

molecules can survive such high temperatures. In reality, the temperature around 5000 K sets after ~ 10's microseconds of plasma evolution; thus a 0–1 μs window in simulations correponds to ~ 10–11 μs window on a real time scale. Even though the initial plasma conditions are far from real, this does not critically affect the spatial distribution of plasma species reached by the moment when all shocks were gone and plasma homogenized and thermalized. The final spatial distributions is similar whether simulations are started from realistically high temperature and go through a long run of ~ 10 μs to reach a final temperature of, e.g., 2000 K or simulations are started from unrealistically low temperature and go through a short run of ~ 1 μs to reach the same temperature. Different initial temperatures (i.e. internal energies) will affect the plasma expansion speed and final plasma size but distributions of molecules and condensate (the point of our interest) will have similar pattern over the plume volume. This is indirectly confirmed by our earlier simulations [34, 35] where higher initial temperatures and longer run times were used.

Figure 3c, d show that significant amount of condensed boron (both liquid and solid) form in the peripheral zone of the plasma. A condensate from this zone can be transported to a substrate (cylinder's wall) by diffusion and convection that is driven by the pressure gradient existing between the plume interior and surroundings (Fig. 3a, b). This process, however, was not modeled in the current work.

Figure 3e, f show the similar 1D expansion of the BCl_3–H_2–CH_4–Ar system. Here, three condensed species coexist; beside the condensed B_4C and C, the condensed B also forms in the plasma bulk. The result is different from that obtained for the static system (Fig. 2b) where only two coexisting solid phases, B_4C and C, were predicted. This implies, unique conditions can be created in laser plasma that favor condensation. Such conditions are difficult to simulate by static equilibrium calculations.

Simulations in spherical symmetry are fast and provide general picture of processes occurring in laser induced plasma. However, spherical plasma is not realistic. Usually, the plasma has an oval shape extended in the direction of the laser beam. We made calculations for an ellipsoidal plasma in 2D symmetry that provide a more realistic space–time distribution of plasma species. Only the system with BCl_3 and methane, 50% (CH_4 + Ar) + 50% (BCl_3 + H_2), was computed as it yields the maximum amount of condensate (as is also inferred from 1D calculations). Namely the formation of solid phase is the ultimate goal of the calculations. Figure 4a–d show the distribution of the condensed B_4C and C at two instants, 200 ns and 910 ns, after beginning the calculations. The plasma initial conditions and stoichiometry are the same as in 1D simulations. It is again obvious from Fig. 4 that the condensate is produced in plasma peripheral zones where conditions are thermodynamically favorable for its formation. A main solid product is crystalline graphite; its concentration is ~ 20-fold higher than that of the other solid component boron carbide. Beside these condensed species, an appreciable amount of gaseous reaction products is formed, i.e. BH_2Cl, $BHCl_2$, HCl, and others (not shown in Fig. 4). The condensed matter can directly adhere to a substrate if the substrate is inert. In many practical situations, however, a substrate is etched by aggressive reactants (like gas is etched by fluorine in our experiment). Therefore, an educated choice of a substrate material may additionally enhance yield of a desired product via not only direct deposition but also surface chemistry.

An attempt to see the condensate with boron in simulations with BF_3 has failed; only formation of solid graphite was observed in system 50% (CH_4 + Ar) + 50% (BF_3 + H_2), the same as in 1D simulations. It is known [57] and follows from these simulations that chemistry of fluorine and fluorides is markedly different from that of "weaker" halogens, e.g. chlorine. Thus, to explain the formation of condensate of boron and its compounds in PECVD with BF_3 a more sophisticated than equilibrium type of modeling is required. For

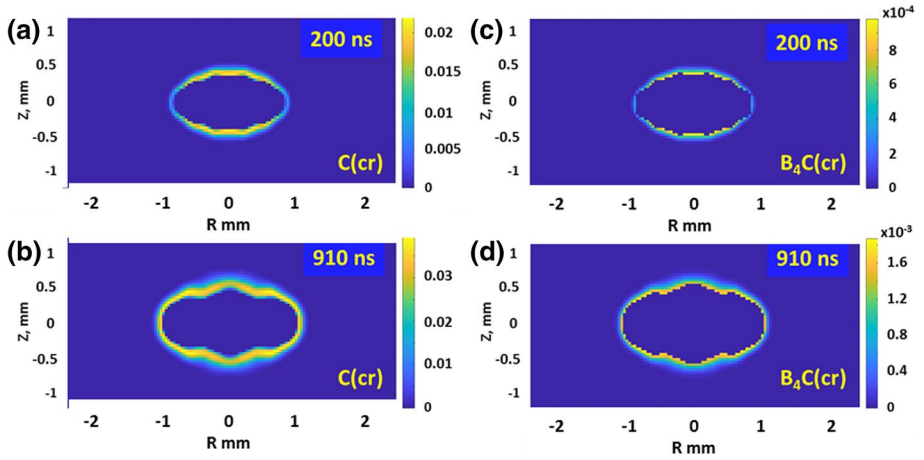

Fig. 4 Dynamic simulations of 2D ellipsoidal (aspect ratio R:Z = 2:1) laser induced plasma containing 50% (CH_4 + Ar) in proportion CH_4:Ar = 3:1 and 50% ($BCl_3 + H_2$) in proportion BCl_3:H_2 = 1:9; **a** condensed C at 200 ns; **b** condensed C at 910 ns; **c** condensed B_4C at 200 ns; **d** condensed B_4C at 910 ns.The color bar shows concentrations in weight %

example, the use of a quasi equilibrium model based on multi temperature functions can fulfill the goal [58]. At present, this model is incompatible with our CFD code and has not therefore been tested.

A next step in modeling "feasible" chemical systems like $BCl_3 + H_2$ that form condensates is the inclusion into the model an interaction between the plasma plume and the reactor wall. This requires introduction of diffusion transport from the plasma plume to reactor walls and specific boundary conditions for the plume-wall interface that will be addressed in future work.

Gas and Solid Analysis Before and After LIDB

A composition of gaseous reaction mixtures before and after the LIDB and solid deposits after the LIDB was studied by methods of optical emission spectroscopy (OES), IR spectroscopy, mass spectrometry, and absorption FTIR spectrometry (solid deposits).

Analysis of Gas Mixtures by OES

A composition of laser-induced plasma was determined by analyzing plasma emission spectra. Spectra from different mixtures taken at different instants of laser-gas interaction are shown in Fig. 5. Lines and bands used for identification of plasma species are listed in Table 2.

For gases with BCl_3 (samples № 1–3 in Table 1), bands of B_2, BH, BCl, and BCl_2 are found in spectra in Fig. 5a–c. Hydrogen lines appear naturally in $H_2 + BCl_3$ and $H_2 + BCl_3$ + Ar and not so naturally in pure BCl_3. Here hydrogen comes likely from the contamination of BCl_3 by HCl (that is typical) and, perhaps, from hydrolysis of BCl_3 by residual water adsorbed on walls of the quartz cylinder. The residual water is also a source of strong emission from BO whose band is seen in the spectrum from sample № 1. Lines

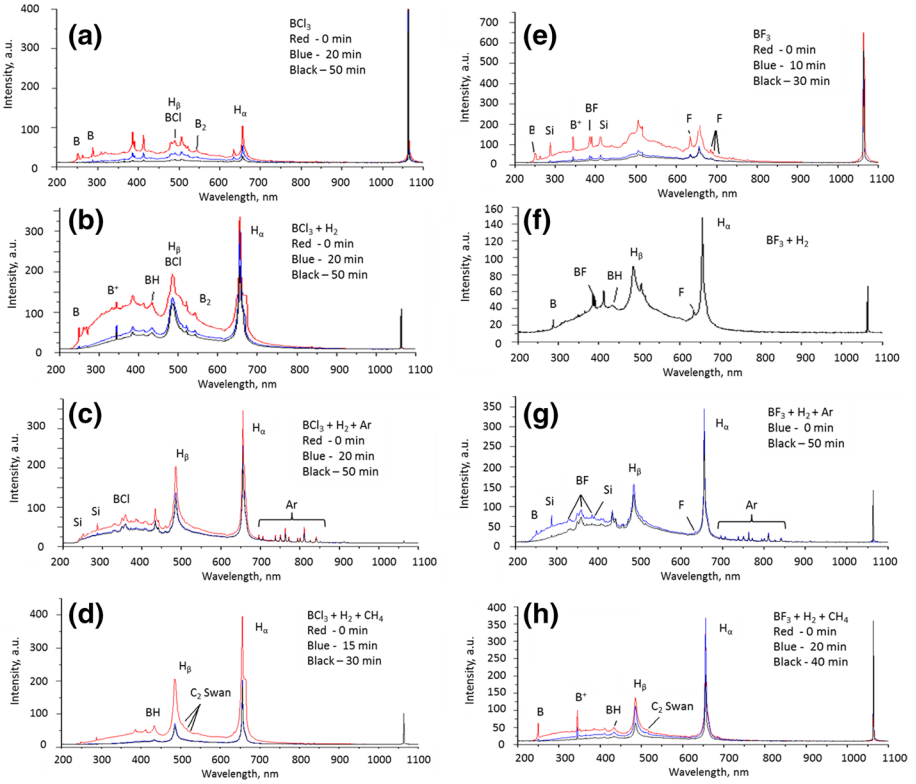

Fig. 5 Emission spectra from laser induced plasma induced in **a** BCl_3; **b** H_2+BCl_3; **c** $H_2+Ar+BCl_3$; **d** $H_2+BCl_3+CH_4$; **e** BF_3; **f** H_2+BF_3; **g** $H_2+Ar+BF_3$; and **h** $H_2+BF_3+CH_4$; all at atmospheric pressure and different duration of laser action

Table 2 Emission lines and bands

Specie	Line/band (nm)	Transition	Source
H_α	656.3	$3d^2D \rightarrow 2p^2P^0$	[59]
H_β	486.1	$4d^2D \rightarrow 2p^2P^0$	[59]
H_γ	434.0	$5d^2D \rightarrow 2p^2P^0$	[59]
B	249.7	$3s^2S \rightarrow 2p^2P^0$	[59]
B+	345.1	$2p^2D^1 \rightarrow 2p^1P^0$	[59]
F	703.8	$3p^2P^0 \rightarrow 3s^2P$	[59]
Cl	837.6	$4p^4D_0 \rightarrow 4s^4P$	[59]
Si	251.6; 288.2	$4s^3P^0 \rightarrow 3p^2D^1$; $4s^1P^0 \rightarrow 3p^2D^1$	[59]
B_2	327.3	$^3\Sigma_u^- \rightarrow X^3\Sigma_g^-$	[60]
BO	384.9	$A^2\Pi_1 \rightarrow X^2\Sigma^+$	[61]
BCl	272; 494	$A^1\Pi \rightarrow {}^1\Sigma^*$; $A^3\Pi_1 \rightarrow {}^1\Sigma^+$	[61]
BH	433.2	$A^1\Pi \rightarrow X^1\Sigma$	[61]
BF	300–340	$A^3\Pi \rightarrow X^1\Sigma^+$	[62]
C_2	516–600	$A^3\Pi_g \rightarrow X'\Sigma^+ {}^3\Pi_u$	[61]
CH	431.4	$A^2\Delta \rightarrow X^2\Pi$	[61]

of Cl at 837 nm, B^+ at 345 nm, Si at 251.6 and 288.2 nm, and bands of BCl at 272 and 494 are identified in spectra in Fig. 5a–c. Si comes from etching the quartz container by halogens. Several bands, e.g. at 330, 350 and 359 nm are not identified.

For gases with BF_3 (samples № 5–7 in Table 1), bands of BF are detected in spectra shown in Fig. 5e–g. A strong B^+ line at 345 nm is seen in the spectrum from pure BF_3; it disappears from spectra of samples with hydrogen. Lines of F are seen in all the spectra between 600 nm and 700 nm; they are the strongest in the spectrum from BF_3. The lines of hydrogen and the band of BO at 385 nm are also present in all the spectra. The bands of BF, BO, and BH are seen in the spectrum from BF_3+H_2 (Fig. 5f). In the spectrum from H_2+BF_3+Ar (Fig. 5g), the same group of non-identified bands at 330, 350 and 359 nm is observed as in H_2+BCl_3+Ar spectra; besides, intense lines of argon appear at 410 and 435 nm.

For the mixtures with methane (samples № 4 and № 8 in Table 1), emission intensities of atoms and molecules of the precursor gas decrease whereas intensities of hydrogen lines increase owing to the dilution of the precursor gas with CH_4. The presence of methane results in the appearance of the Swan C_2 band in the range 516–600 nm and the CH band (Fig. 5d, h) that overlaps with the H_γ line of hydrogen. In the spectra from mixtures containing either BCl_3 or BF_3, the bands of BH and weak bands of BO are present while the bands of B_2 are not. Note the much stronger intensities of B and B^+ lines in the spectra from sample № 8 than from sample № 4; the lines of Si almost disappear from the latter spectrum. These peculiarities point to the different routes of chemical reactions in the mixtures with BCl_3 and BF_3 and methane. The difference in chemistry of BCl_3 and BF_3 is also obvious from MS spectra of reaction products (shown below) that reveal the presence of methyl derivatives that form in the BF_3+CH_4 mixture.

Analysis of Gas Mixtures by IR Spectroscopy

Figure 6 shows the IR spectra of samples from Table 1 before and after multiple breakdown events. The IR spectrum of BCl_3 (samples № 1–4 in Table 1), contains vibrational band ν_3 at 995 and 956 cm^{-1} belonging to boron isotopes and a weak band of HCl at 2900 cm^{-1} (Fig. 6a–d). The ν_3 band almost disappears from post-irradiation spectra of gases (black spectra in Fig. 6); instead, bands of reaction products appear. In the IR spectrum of pure BCl_3 (Fig. 6a), the HCl band is seen, in agreement with the OES spectrum from the same sample. A series of new bands appears at low frequencies 1267, 913, 800–845, 690 и 547 cm^{-1}, and a wide band appears at high frequency peaking at 2980 cm^{-1}. Their possible origin is discussed below.

The IR spectrum of mixture BCl_3+H_2 (Fig. 6b) after the irradiation contains bands $\nu_3=892$ cm^{-1} and $\nu_2=1089$ cm^{-1} of BH_2Cl and bands at 1600 and 2600 $cm^{-1}$of diborane B_2H_6. The intensities of the low frequency bands at 1100, 900 and 815 cm^{-1} decrease (likely, due to the dilution of BCl_3 by H_2) while the intensity of the high frequency band of HCl increases. The weak unidentified band at 2980 cm^{-1} is observed. In the spectrum from sample № 4 (Fig. 6d), the pronounced bands of methane at 1300 and 3000 cm^{-1} are clearly seen along with the intense bands of acetylene at 730 and 3300 cm^{-1}.

The IR spectra of BF_3 and its mixtures with hydrogen and methane (Fig. 6e–h) show the fundamental vibration bands $\nu_2=718$ and 691 cm^{-1}, $\nu_3=1505$ and 1453 cm^{-1} as well as a composite band $\nu_1+\nu_3=2385$ and 2386 cm^{-1} from isotopic modifications of BF_3. After irradiation, these bands almost disappear and the new bands appear at 1270, 940, and 820 cm^{-1}, similar to BCl_3. Note these bands are also seen in the spectrum

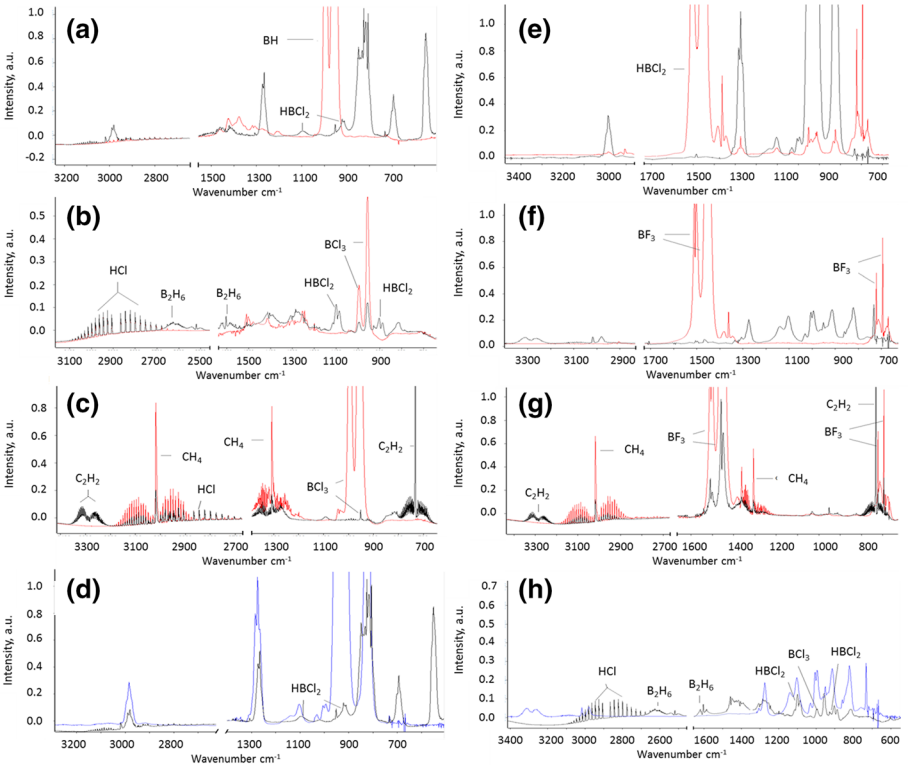

Fig. 6 IR spectra of **a** BCl_3 at 20 torr; **b** BCl_3+H_2 at 200 torr; **c** $BCl_3+H_2+CH_4$ at 250 torr; **d** ClF_3 and BF_3 at 20 torr; **e** BF_3 at 20 torr; **f** BF_3+H_2 at 100 torr; **g** $BF_3+H_2+CH_4$ at 250 torr; **h** BCl_3+H_2 at 204 torr and BF_3+H_2 at 100 torr. The red and black lines in panels a–c and e–g correspond to spectra taken before and after laser irradiation, correspondingly

from pure BF_3 (sample № 4) and have low intensities. In the high frequency range, a band at 2980 cm^{-1} is seen, which is also seen in the BCl_3 spectra, and the two bands at 3015 cm^{-1} (narrow) and 3300 cm^{-1} (wide). The latter bands may come from the products of the reaction of aggressive gases with seal gaskets placed between the reactor wall and windows. In the spectrum from sample № 7 with methane (Fig. 6g), the residual absorption bands at 1454 cm^{-1} (BF_3), 1300 and 3000 cm^{-1} (CH_4) and new strong bands of acetylene at 730 and 3300 cm^{-1} are observed. Molecules of diborane, B_2H_6, as well as HF and BF_2H are not detected as opposed to mixtures with BCl_3. Instead, all the IR spectra from BF_3 mixtures show traces of SiF_4 that come from etching the reactor wall by fluorine.

The unidentified bands at 700–1400 cm^{-1} and 2980 cm^{-1} in the spectra from both the BCl_3 and BF_3 containing mixtures likely belong to products of plasma chemical reactions with unknown contaminants in the precursor halides (see, e.g. Fig. 6e). Based on the OES spectra, which show the hydrogen lines and BO band, one can assume that these compounds contain groups B–O and B–H.

Analysis of Gas Mixtures by Mass Spectrometry

Mass spectrometry (MS) confirms the data obtained by optical spectroscopy and complement them. Figure 7a–f present the MS spectra of samples listed in Table 1 before and after laser irradiation.

The MS spectra of BCl_3 and its mixtures with other gases do not show peaks from BCl_3^+ after the laser irradiation (Fig. 7a–c). In sample № 2, BCl_3+H_2, the peak of diborane, $B_2H_6^+$, and the intense peak of HCl^+ are observed. In sample № 4, $BCl_3+H_2+CH_4$ (Fig. 7c), the reaction products include acetylene $C_2H_2^+$ and ethylene $C_2H_4^+$ as well as HCl^+; the HCl^+ peaks become much more intense in the post-irradiation mixture.

In contrast to BCl_3, in the MS spectra of BF_3, the peaks of BF_3^+ do not disappear completely after the laser irradiation (Fig. 7d). In the mixtures with H_2 and CH_4, peaks of diborane are seen (Fig. 7e, f); they are much stronger in the initial BF_3 than in post-irradiated BF_3 (Fig. 7d). In the mixture with methane, acetylene and ethylene form (Fig. 7f). Small amounts of HF and SiF_4 appear in all post-irradiated samples with BF_3.

The composition of the gas phase determined spectroscopically agrees well with that calculated on the basis of the equilibrium plasma chemical model. The calculations predict formation of molecules HCl and BCl_2H at temperatures below 500 K and the IR spectroscopy confirms that. Note, the synthesis of BCl_2H molecules from the BCl_3+H_2 mixture by photolysis of BCl_3 with a CO_2 laser was described in [63]. In contrast, the theory predicts that formation of analogous molecules HF and BF_2H in BF_3 systems can occur only at elevated temperatures and therefore these molecules are not seen in the IR spectra taken at room temperature. The presence of lines and bands of B, BH, BCl, Cl, BF, F, and H in the OES spectra is also confirmed by computations. Based on the results of the IR and MS analyses, the efficiency of conversion of a precursor gas into products is close to 100% for BCl_3 and is about 80% for BF_3.

However, the main goal of CVD LIDB is to obtain deposits of elemental boron or/and boron-containing products. LIDB in our experiment resulted in deposition of condensate

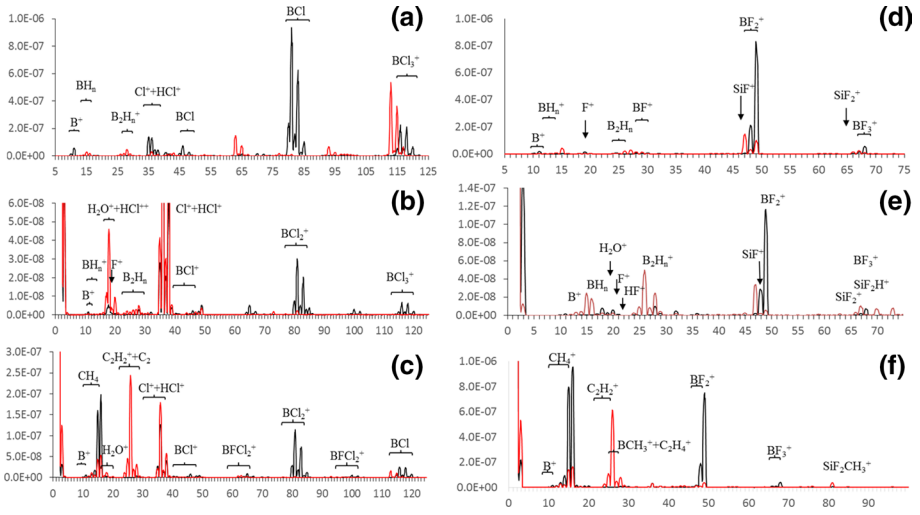

Fig. 7 MS spectra of **a** BCl_3; **b** BCl_3+H_2; **c** $BCl_3+H_2+CH_4$; **d** BF_3; **e** BF_3+H_2; and **f** $BF_3+H_2+CH_4$. The black and red correspond to spectra taken before and after laser irradiation, correspondingly

on the reactor wall in the form of a thin film or powder. The amount of the deposit did not exceed 30 mg for a given laser pulse energy, irradiation time, and reactor volume; besides, the deposit was distributed over a large area. In this pilot experiment, the amount of the deposit sufficient for further analysis could only be collected for sample № 4, $BCl_3 + H_2 + CH_4$.

At present, structural analysis by X-ray diffraction was not available and the deposit was characterized by only the FTIR method (Fig. 8). Based on the position of the strongest bands around 1000 cm^{-1} the part of the deposit was attributed to $B_{6,5}C$ [64].The other part of the deposit is likely a condensed boron; this is implied from the presence in the spectrum of the B–B bond at 1350 cm^{-1} (Fig. 8). The crystalline and amorphous graphite was not identified by the FTIR but its presence could be inferred from the visual analysis of the deposit, which showed the presence of soot particulates. Thus, all three condensed phases predicted by the CFD-chemical calculations of LIBD in the $H_2 + BCl_3 + CH_4 + Ar$ mixture (Fig. 3, 4 and 5) are very likely to be created in the experiment. The yield of the solid deposit and its precise composition are not yet fully characterized; this analysis is planned for the near future.

Conclusions

The possibility of deposition of solid materials from a laser-induced plasma created in reactive precursor gases is investigated. In the 1980th, the method (tabbed as CVD LIDB chemical vapor deposition by laser-induced dielectric breakdown) have demonstrated its high potential and since then was abandoned. Here, we bring it back to life in a search for an economic and simple method for obtaining pure isotopic compounds from isotopically enriched (and expensive) gaseous precursors. In this proof-of-principle work, no isotopic compounds have yet been used; instead a simple breakdown in reactive gas mixtures was studied both theoretically and experimentally. The gases were boron chloride and boron fluoride mixed with hydrogen, argon, and methane.

In the theoretical part, the *static* equilibrium chemistry calculations were performed and showed the condensed phase of boron is thermodynamically possible in chemical system $BCl_3 + H_2 + Ar$ and the condensed phases of boron, boron carbide, and carbon are

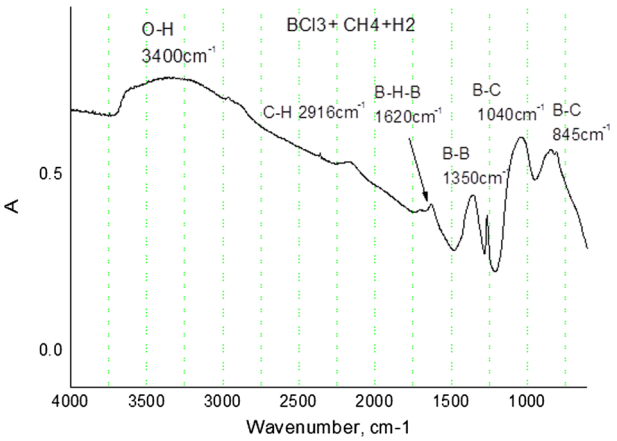

Fig. 8 IR absorption spectrum of solid deposit from the mixture H_2:BCl_3:CH_4 = 9:1.5:1

thermodynamically favorable in $BCl_3+H_2+CH_4$ system. In contrast, out of all BF_3 systems, the solid phase was allowed only in one of them, $BCl_3+H_2+CH_4$, and only in the form of solid carbide. This result contradicts the experimental data obtained in PECVD with fluorides where the formation of solid deposits other than carbon was observed. The conclusion is drawn that a more sophisticated than equilibrium model is required to model chemistry in fluorine-containing systems.

The *dynamic* calculations of the expanding plasma plume were carried out using the fluid dynamic numerical algorithm based on the Navier–Stokes equations coupled with the open source chemical algorithm based on the minimization of Gibbs free energy. The space and time distribution of the reactants and products as well as their aggregate states were assessed by modeling the 1D (spherical) and 2D (oblate) expansions of the plasma plume. The three coexisting condensed phases, B(L), C(gr), and B_4C(cr) were predicted for the dynamic plasma plume. A zone of the maximum concentration of the condensed species is located in the peripheral part of the plasma. The deposition can conveniently be realized on a substrate placed near the plasma plume, e.g. inside a small diameter enclosure.

The chemical reactor consisting of two concentric cylinders was used in LIDB experiment. The plasma was induced in eight gas mixtures: BCl_3, H_2+BCl_3, $H_2+Ar+BCl_3$, $H_2+BCl_3+CH_4$, BF_3, H_2+BF_3, $H_2+Ar+BF_3$, and $H_2+Ar+BF_3$. The gases were analyzed before, during, and after the laser irradiation by optical (OES, IR) and mass spectrometry (MS). The results showed the compositions close to that predicted by the models. The conversion of precursor gases BCl_3 and BF_3 into reaction products was estimated to be 100% for BCl_3 and 80% for BF_3.

Solid deposits were obtained from all the reaction mixtures but only mixture $H_2+BCl_3+CH_4$ was analyzed by FTIR as it provided sufficient for analysis amount of the deposit (30 mg). The FTIR spectrum revealed three condensed phases that were also predicted by the dynamic LIDB model: solid boron, boron carbide, and graphite.

To resume, the simple equilibrium plasma model was applied to the mixture of volatile BCl_3 with H_2 and CH_4 and yielded the results in agreement with experiment. The model can be useful for optimizing experimental conditions and increasing efficiency of CVD LIBD. A more sophisticated model is needed for fluorides because the equilibrium model is unable to predict solid phases seen in experiment. In general, the calculations and preliminary experimental results imply CVD LIBD can be the promising method for efficient conversion of gaseous enriched precursors into pure elemental isotopes and their isotopic compounds.

Acknowledgments The authors are very grateful to Prof. U. Panne and Dr. K. Rurack for the support of this project. P.S. acknowledges the DAAD/2019 grant 9165134. P.S., R.A. and A.A. acknowledge the RSF Grant No 20-13-00035 for basic support as well as the Russian Ministry of Education and Science (subject 0095-2019-0008) for the partial support. The authors are grateful to Melsytech LTD (D. Stepanov, A. Stepanov, O. Yeremeykin) for the technical support.

References

1. Martins R, Aguas H, Cabrita A, Tonello P, Silva V, Ferreira I et al (2001) Sol Energy 69:263–269
2. Pryce Lewis HG, Edell DJ, Gleason KK (2000) Chem Mater 12:3488–3494
3. Cui L, Chen J, Yang B, Jiao T (2015) Nanoscale Res Lett 10:1–6
4. Kornev RA, Sennikov PG, Konychev DA, Potapov AM, Chuvilin D, Yunin P, Gusev SA (2016) J Radioanal Nucl Chem 309:833–840
5. Vasudev MC, Anderson KD, Bunning TJ, Tsukruk VV, Naik RR (2013) ACS Appl Mater Interfaces 5:3983–3994

6. Hamedani Y, Macha P, Bunning TJ, Naik RR, Vasudev MC (2016) In: Chemical vapor deposition-recent advances and applications in optical, solar cells and solid state devices. InTech, p 247
7. Baum TH, Comita PB (1992) Thin Solid Films 218:80–94
8. Roy SK (1988) Bull Mater Sci 11:129–135
9. Baranauskas V, Mammana CIZ, Klinger RE, Greene JE (1980) Appl Phys Lett 36:930
10. Bäuerle D, Irsigler P, Leyendecker G, Noll H, Wagner D (1982) Appl Phys Lett 40:819–821
11. Hanabusa M, Namiki A, Yoshihara K (1979) Appl Phys Lett 35:626
12. Ann E. Stanley (1987) US Patent 4681640
13. Jervis TR (1985) J Appl Phys 58:1400–1401
14. Jervis TR, Newkirk LR (1986) J Mater Res 1:420–424
15. Ronn AM (1976) Chem Phys Lett 42:202–204
16. Lin ST, Ronn AM (1978) Chem Phys Lett 56:414–418
17. Draper CW (1980) Met Trans 11A:349–351
18. Shin SM, Draper CW, Mochel ME, Rigsbee JM (1985) Mater Lett 3:265–269
19. Draper CW (1980) J Phys Chem 84:2089–2090
20. Subramanian C, Suri AK, Murthy TSRCh (2010) Int Mater Rev 55:4–40
21. Thevenot F (1990) J Eur Ceramic 6:205–225
22. https://www.tracesciences.com/b.htm
23. Bendel P (2005) NMR Biomed 18:74–82
24. Sennikov PG, Kornev RA, Abrosimov NV (2015) J Radioanal Nucl Chem 306:21–30
25. Bluhm H, Schreiber L (2019) IEEE international symposium on circuits and systems (ISCAS). 26–29 May 2019 Supporo. https://doi.org/10.1109/iscas.2019.8702477
26. Weber JR, Koehl WF, Varley JB, Janotti A, Buckley BB, Van de Walle CG, Awschalom DD (2010) Proc Nat Acad Sci 107:8513–8518
27. Schraml J, Bellama JM (1976) ^{29}Si-Magnetic resonance in the determination of organic structures by physical methods V. 6. Academic Press, New York
28. Bellotti E (2006) J Phys Conf Ser 39:338
29. Liu ZT, Zhu JZ, Xu NK, Zheng XL (1997) Jpn J Appl Phys 36:3625–3628
30. Stephenson CA, O'Brien WA, Penninger MW, Schneider WF, Gillett-Kunnath M, Zajicek J, Yu KM, Kudrawiec R, Stillwell RA, Wistey MA (2016) J Appl Phys 120:053102
31. https://cearun.grc.nasa.gov. Accessed 15 Apr 2020
32. Smith WR, Missen RW (1982) Chemical reaction equilibrium analysis: theory and experiment. Wiley, New York
33. Shabanov SV, Gornushkin IB (2018) Appl Phys A 124:716
34. Shabanov SV, Gornushkin IB (2014) Spectrochim Acta, Part B 100:147–172
35. Shabanov SV, Gornushkin IB (2016) Appl Phys A 122:676
36. Gravelle DV, Beaulieu M, Boulos MI, Gleizes A (1989) J Phys D Appl Phys 22:1471–1477
37. van Dijk J, Kroesen GMW, Bogaerts A (2009) J Phys D Appl Phys 42:190301
38. Drawin HW (1976) Pure Appl Chem 48:133–153
39. Griem HR (1997) Principles of plasma spectroscopy. Cambridge University Press, Cambridge
40. Cristoferetti G, Tognoni E, Gizzi LA (2013) Spectrochim Acta, Part B 90:1–22
41. Shabarova LV, Plekhovich AD, Kut'in AM, Sennikov PG, Kornev RA (2019) High Energy Chem 53:148–154
42. Gornushkin IB, Shabanov SV, Sennikov PG (2019) Plasma Chem Plasma Proc 39:1087–1102
43. Reinisch G, Leyssale J-M, Bertrand N, Chollon G, Langlais F, Vignoles G (2008) Surf Coat Technol 203:643–647
44. Reinisch G, Vignoles GL, Leyssale J-M (2011) J Phys Chem A 115:11579–11588
45. Sennikov PG, Kornev RA (2017) Shishkin AI 37:997–1008
46. Donaldson JG, Stephenson JB, Cochran AA (1973/74) Electrodepos Surface Treat 2:149–163
47. Casavola AR, Colonna G, Capitelli M (2009) Plasma Sour Sci Technol 18:025027
48. Capitelli M, Armenise I, Bruno D, Cacciatore M, Celiberto R, Colonna G, DePascale O, Diomede P, Esposito F, Gorse C, Hassouni K, Laricchiuta A, Longo S, Pagano D, Pietanza D, Rutigliano M (2007) Plasma Sour Sci Technol 16:S30–S44
49. Tuttafesta M, Pascazio G, Colonna G (2016) Comput Phys Commun 207:243–257
50. Morel V, Bultel A (2010) Ch´eron BG. Spectrochim Acta B 65:830–841
51. Morel V, Bultel A, Annaloro J, Chambrelan C, Edouard G, Grisolia C (2015) Spectrochim Acta B 103–104:112–123
52. Villars DS (1959) J Phys Chem 60:521–525
53. Cruise DR (1964) J Phys Chem 68:3797–3802
54. Colonna G (2007) Comput Phys Commun 177:493–499

55. Koukkari P, Pajarre R, Pakarinen H (2002) J Solut Chem 31:627. https://doi.org/10.1023/A:1020201909118
56. Holstein WL (1992) Prog Cryst Growth Char 24:111–211
57. Gutmann V (1967) Halogen chemistry. Elsevier, Amsterdam
58. Kut'in AM, Polyakov VS In (2007) XVI international conference on chemical thermodynamics in Russia (RCCT 2007) abstracts Suzdal July 1–6 Vol 2:514–515
59. https://www.nist.gov/pml/atomic-spectra-database
60. Hachey M, Karna SP, Grein F (1992) J Phys B 25:1119
61. Pearse RWB, Gaydon AG (1963) The identification of molecular spectra, 3rd edn. Chapman and Hall, London
62. Lebreton J, Ferran J, Marsigny L (1975) J Phys B Mol Phys 8:L465–L466
63. Rockwood SD, Hudson JW (1975) Chem Phys Lett 34:542–545
64. Lifshitz EW, Shewyakowa EP, Ostapenko IT, Berznyak EP, Saenko LA (2004) Topics in nuclear science and technology (Voprosyatomnoy nauki i tekhniki) No. 3 Series 85:19–22 (in Russian)